Chapter 3

Cathode Materials for Lithium Sulfur Batteries: Design, Synthesis, and Electrochemical Performance

Lianfeng Duan, Feifei Zhang and Limin Wang

Additional information is available at the end of the chapter

http://dx.doi.org/10.5772/62439

Abstract

With the rapid development of electronic devices, portable electronics, and electric vehicles, the energy density and cycle life of LIBs are insufficient for the demands. Based on the reaction mechanisms, lithium-sulfur (Li-S) batteries have a high specific capacity of 1672 mAh/g, with a theoretical energy density up to 2600 Wh/Kg. However, the sulfur cannot serve as cathode individually because of its isolation nature and soluble compounds, which necessitates a second component as a conducting matrix and sulfur host. Thus, sulfur cathodes have diversified through microstructure designing with various materials, including inorganic compounds, polymers, carbon materials, and their hybrids, which should be satisfied several essential requirements, such as high stable incorporation with sulfur, high electrical conductivity of electrode materials, and loose framework to suffer the volume expansion of cathode during charge-discharge process. These investigations may provide the effective routes to prepare different new cathode materials with unique structures and morphologies for Li-S batteries, which improve cycling stability, coulombic efficiency, and rate capacity of the electrode at higher current density.

Keywords: Cathode Materials, Li-S Batteries, Composites, Electrochemical Property, Electrochemical Performance

1. Introduction

With the fantastic development of electronic devices, ranging from portable electronics to electric vehicles, widespread concern for high-power and high-energy density rechargeable batteries has been paid in the new century [1, 2]. In particular, lithium-ion batteries (LIBs) are promising energy storage devices and achieved remarkable success in portable electronics market

during the past two decades [3]. However, the traditional cathode materials based on the lithiated transition-metal oxide and phosphate have relative low energy densities (theoretically, 350–400 Wh kg^{-1}, practically, 100–220 Wh kg^{-1}) and insufficient for the upcoming large-scale energy demands [4]. In addition, most LIBs are too expensive to be economical for large-scale applications and make the price of electric vehicles prohibitively expensive for the ordinary consumers [5]. However, the limited electrochemical stability window of the currently available liquid electrolytes makes it difficult to increase the cathode operating voltage beyond 4.3 V. Also, the capacities of the insertion-oxide cathodes have reached a limit of 250 mA h g^{-1}. On the other hand, the capacity of the graphite anode is also limited to 370 mA h g^{-1}. Therefore, it is necessary to explore novel rechargeable systems based on new chemical theory, such as lithium-sulfur (Li-S) batteries, Li-air batteries and sodium-sulfur batteries, or new electrode materials with high energy densities, like multi-electron reaction materials and high voltage materials, to meet the requirements of sustainable energy fields.

Li-S batteries based on elemental sulfur as cathode and metal lithium as anode have attracted considerable attention because of their high theoretical specific capacity of 1672 mA h g^{-1} and high theoretical energy density of 2600 Wh kg^{-1} [2]. Moreover, as a byproduct of petroleum refinement or direct extraction from sulphate minerals, sulfur with the merits of abundant resources and environment friendly are beneficial for sustainable development [6]. The history of Li-S batteries development dated back to 1962 when Herbet and Ulam first used sulfur as a cathode material in electric dry cells and storage batteries [7]. Later, Argonne national laboratory developed a high-temperature Li-S system in 1967 [8]. However, the safety problems of high-temperature system remained challenging and limited applications, until E. Peled's group reported the electrochemical characteristics of sulfur in organic electrolytes at room temperature [9, 10]. Since then, more and more researches focused on the developments of high energy density, long-life times and safety Li-S systems.

2. Principles and challenges of lithium-sulfur batteries

2.1. The charge-discharge mechanism of Li-S batteries

Unlike the intercalation-deintercalation mechanism of traditional rechargeable LIBs, a Li-S cell undergoes a reduction-oxidation reaction and starts with discharge due to the charged state of sulfur. During the discharge reaction, lithium metal is oxidized to give up lithium ions and electrons. The lithium ions move from negative electrode to positive electrode through the internally electrolyte while the electrons circulate through the external electrical circuit, and thereby an electrical current is generated. Elemental sulfur at the positive electrode is reduced to lithium sulfide (Li_2S) by accepting the lithium ions and electrons [1]. The reverse reactions will occur during charge process. The discharge reactions can be described as follows:

Negative electode:

http://dx.doi.org/10.5772/62439

$$2Li \rightarrow 2Li^{+} + 2e^{-}$$

Positive electrode:

$$S + 2Li^{+} + 2e^{-} \rightarrow Li_2S$$

Overall discharge reaction:

$$2Li^{+} S \rightarrow Li_2S$$

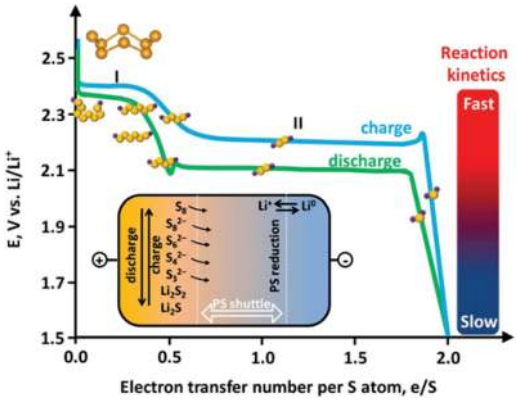

Figure 1. Electrochemistry of sulfur showing an ideal charge-discharge profile. Inset: polysulfide shuttle [13].

In fact, this reaction is a multi-step process which can be observed from the typical constant-current discharge curve of Li-S cell. As shown in **Figure 1**, there are two voltage plateaus in the first discharge curve. The higher voltage plateau at about 2.3 V is associated with the open ring reduction of the cyclic-octasulfur (S_8, most common stable form among sulfur allotropes) [14] to various long-chain (high-order) soluble lithium polysulfides (Li_2S_n, $4 \leq n \leq 8$), which proceeds through multiple steps [15, 16]:

$$S_8 + 2e^{-} \rightarrow S_8^{2-}$$

$$3S_8^{2-} + 2e^{-} \rightarrow 4S_6^{2-}$$

$$S_6^{2-} + 2e^{-} \rightarrow 3S_4^{2-}$$

The following plateau at about 2.1 V relates to the further reduction of these polysulfides to short-chain (low-order) insoluble lithium polysulfides (Li_2S_n, $n < 4$) and finally, lithium sulfide (Li_2S) [13].

$$S_4^{2-} + 4Li^+ + 2e^- \rightarrow 2Li_2S_2$$

$$Li_2S_2 + 2Li^+ + 2e^- \rightarrow 2Li_2S$$

During the following charge process, Li_2S is converted back into to intermediate lithium polysulfides, while the formation of S_8 does not usually occur [17, 18], the two charge voltage plateaus are normally overlapped with each other [1].

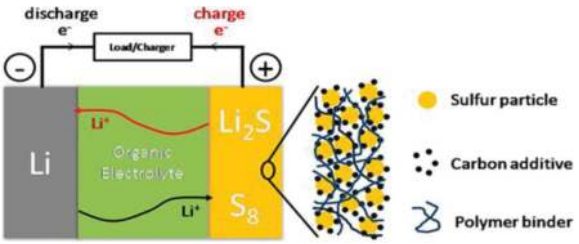

Figure 2. Structure scheme of Li-S battery [11].

2.2. The structure of Li-S batteries

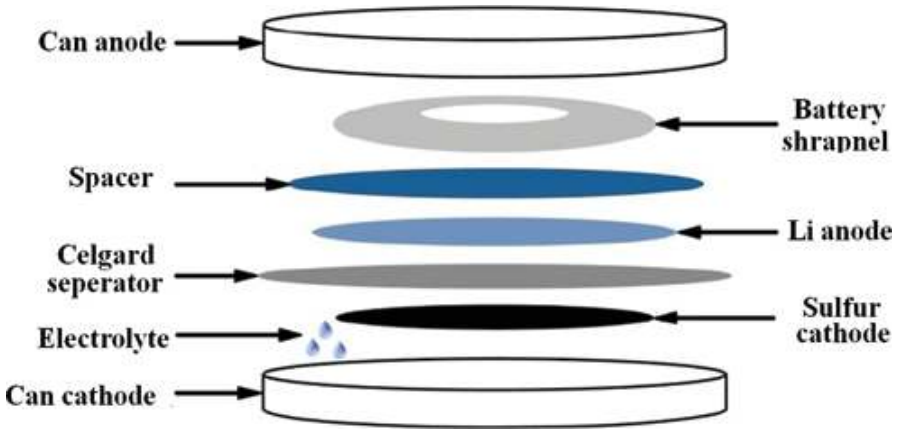

Figure 3. The schematic and assembling of CR2025 type button cell.

A Li-S cell is an electrochemical storage device through which electrical energy can be stored in sulfur electrodes. As shown in **Figure 2**, a conventional Li-S cell is composed of sulfur composite as the cathode, lithium metal as the anode, and separated an organic lithium solution as the electrolyte [12]. Because of the highly electrically and ionically insulating nature of sulfur, it must be kept at immediate contact with conductive additive to enable a reversible

http://dx.doi.org/10.5772/62439

electrochemical reaction, then the cathode contains elemental sulfur, conductive carbon, and polymer binder. **Figure 3** is the assembling schematic of Li-S cell (CR2025 type button).

2.3. The challenges of sulfur cathode

Although the Li-S batteries exerted considerable superiorities when considering the high energy density and low cost, there are still many challenges of cathode materials associated with the practical applications.

Firstly, the cathode materials must be added with plentiful conductive agent to increase the electrical and ionic conductivity of cathode due to the insulating nature of sulfur (5×10^{-30} S cm^{-1}) [17], which resulting in low specific energy density of the whole cell. In addition, the last step of converting Li_2S_2 to Li_2S is difficult and is impeded by slow solid-state diffusion and poor electrical conductivity of Li_2S (3.6×10^{-7} S cm^{-1}) [15, 19]. Therefore, the active material utilization is low deriving from the incomplete discharge.

Secondly, the volume variation of sulfur particles during the charge and discharge process is large. Sulfur has a density of 2.03 g cm^{-3}, while Li_2S is lighter with 1.66 g cm^{-3}. As a result, the volume expansion within cathode when sulfur is fully converted to Li_2S is as large as 80% [13]. This volume change leads to serious cathode pulverization and thus fast capacity decay.

Thirdly, the polysulfide species (S_8^{2-}, S_6^{2-}, and S_4^{2-}) which are produced in the charge-discharge process are easily soluble in the electrolyte and diffuse freely from the cathode to anode driven by a concentration gradient (**Figure 2**, inset). Then, they react with lithium anode and reduced to short-chain polysulfides. The insoluble Li_2S_2/Li_2S deposits on the lithium anode can react with polysulfide ions again, yielding soluble medium-chain ions, which could diffuse back to cathode where they are reoxidized [20]. The mobile polysulfides therefore circulate between cathode and anode, driving the charging time of the cell towards infinity. This phenomenon, which is the main reason caused low coulombic efficiency and self-discharge of the cell, is so-called "polysulphide-shuttle" [21]. Additionally, these soluble species can be reduced to Li_2S insulating layer at the lithium anode surface, passivating the anode and leading to material loss and impedance increase. Moreover, the insoluble and electrically insulating Li_2S_2/Li_2S can be formed and precipitated out at the cathode surface. Once a thin Li_2S layer completely covers the whole cathode, further lithiation will be largely impeded and resulting in the low active utilization and coulombic efficiency. With the cycling going on, the dissolution and precipitation process will change the morphology of the cathode each cycle, which induces serious capacity fading and degrades the cycle life.

Excellent sulfur cathodes for high capacity and great cycling stability should contain several desired features: (1) a closed structure to encapsulate polysulfides efficiently, improving sulfur-electrolyte contact, (2) good conductivities achieved, for example, by mixing conductive materials in the cathode, (3) a loose structure to provide sufficient space to accommodate sulfur volumetric expansion and preserve the morphology of electrodes during transportation of electrons and Li ions.

In this chapter, different nanosized and nanostructured sulfur-based cathodes based on morphologies and compositions of the electrode are presented, including (1) sulfur-impreg-

nated core-shell hierarchical porous carbon (HPC) composites; (2) sulfur/graphene nanosheets (GNS) composite; (3) sulfur@rGO composite with a saccule-like structure; (4) C-S@PANI composite with polymer spherical network structured. With such systematic discussion, we aim to provide a better and comprehensive understanding in this area. Although the crystal structures have boosted remarkable progress in the electrochemical property as cathode for Li-S batteries, it is more important to design and synthesis special and novelty cathodes in order to promote cycling stability, improve excellent capacity density, and rate capability by simple and environmental friendly processes. With such systematic discussion, we aim to provide a better and comprehensive understanding in this area.

3. Sulfur-impregnated core-shell hierarchical porous carbon composites as the cathode material for Li-S batteries

In order to advance Li-S batteries, a variety of strategies have been carried out to address these problems, including the optimization of electrolyte or additives [22], the preparation of the sulfur-conductive polymer composites [23], sulfur-carbon composites [24–26], and the protection of lithium anode. Among these approaches, fabricating sulfur/carbon composite cathodes with sulfur embedded within conductive carbon frameworks has been proven promising. In particular, carbon materials with porosity, high conductivity, large pore volume, and high surface area (such as carbon nanotubes, mesoporous and microporous carbon, hollow carbon, etc.) are proved to be effective and facile substrates for encapsulating polysulfides and improving sulfur-electrolyte contact [25–27].

3.1. The schematic representation of core-shell HPCs-S

Unique core-shell sphere with a radially aligned HPC shell is synthesized as the host of sulfur (**Figure 4a**). Both of the outer shell and inner core are highly porous framework, providing a fine carbon matrix for sulfur loading. Subsequently, the sulfur is impregnated by heating a mixture of the HPC composites and sulfur (HPCs-S) in a sealed inert atmosphere, forming core-shell HPCs-S-H composite (**Figure 4b**). The sulfur is not merely impregnated in the pores, but also deposited on the external of the spheres. Further treatment is carried out by dispersing the HPCs-S-H composite in the toluene to dissolve partial sulfur to obtain HPCs-S composite. The core-shell structure and open pore mouths of carbon sphere are maintained in HPCs-S composite. For this unique structure, sulfur is mainly distributing over the core area of HPCs, the shell of HPCs with void pores are serving as a retard against the dissolution of lithium polysulfides.

http://dx.doi.org/10.5772/62439

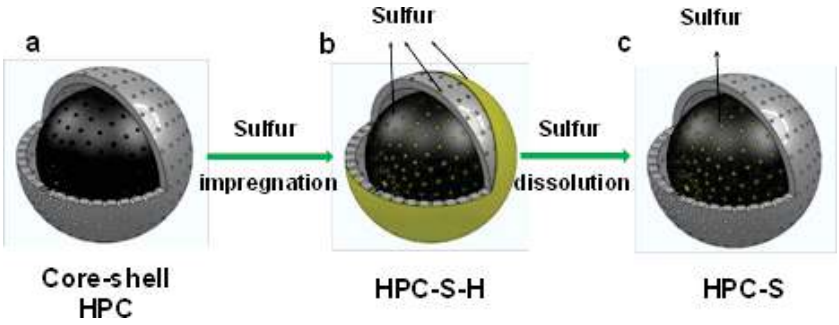

Figure 4. Schematic illustration of the procedure used to fabricate core-shell HPCs-S-H and HPCs-S composites [28].

3.2. Morphology and microstructure characterization of core-shell HPCs-S

Figure 5a shows the polymer-silica-surfactant (PSS) spheres are uniform solid spheres with perfectly smooth surface. After carbonized at 600°C and etched with HF solution, HPCs with pores on surface are obtained, and the dimension is 600~700 nm (**Figure 5b**). When impregnated with sulfur, a layer of sulfur particles deposited on the external of the spheres is clearly seen from SEM image of HPCs-S-H (**Figure 5c**). After the dissolution process, the sulfur aggregated on the surface vanishes and the porous morphology reappears (**Figure 5d**).

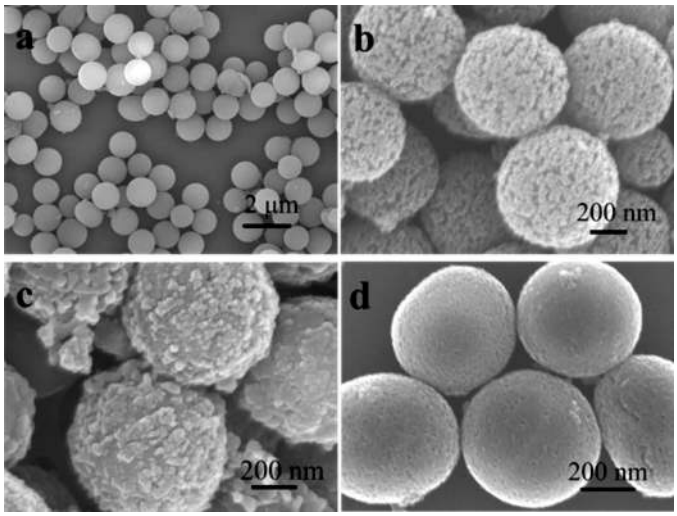

Figure 5. SEM images of the as-synthesized (a) PSS composite, core-shell (b) HPCs, (c) HPCs-S-H and (d) HPCs-S composite [28].

TEM images of HPCs are shown in **Figure 6**. The core-shell HPCs with highly porous structure can be obviously seen from **Figure 6a**. The dimension of spheres is in the range of 600–700 nm, and the thickness of shell is about 40 nm. TEM image in **Figure 6b, c** show that the distance of the gap between the shell and the core is about 8.3 nm. The outer shell is shucked and the inner mesopores are obviously observed. TEM image of the shell area which shows in **Figure 6d** exhibits that micropores and mesopores uniformly distribute through the shell area.

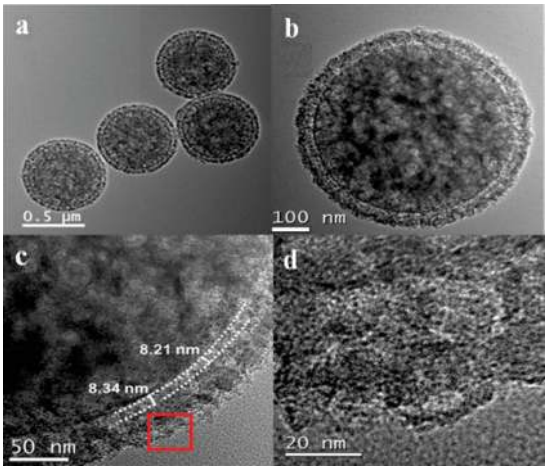

Figure 6. TEM images of the as-synthesized core-shell, (a) and (b) HPCs, (c) the gap between the shell and core, (d) the outer shell of an HPCs [28].

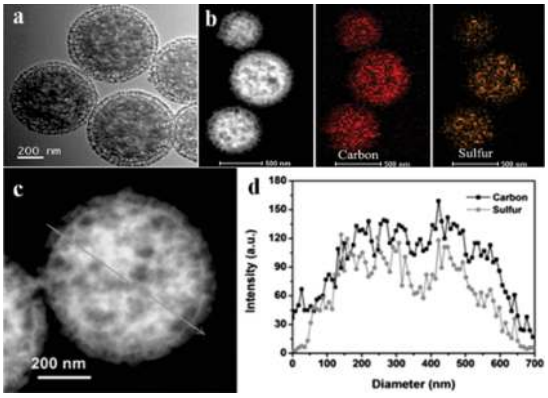

Figure 7. TEM images of the as-synthesized core-shell (a) HPCs-S composite, (b) magnified image of separate core-shel HPCs-S particles and the corresponding EDS elemental mapping of carbon and sulfur, (c) dark field TEM image of HPCs-S; (d) the linear EDX element distributions of sulfur and carbon along the arrow line of (c) [28].

http://dx.doi.org/10.5772/62439

Figure 7 is TEM images and elemental analysis of the as-synthesized core-shell HPCs-S composite. From this Figure, comparing with the HPCs, the core-shell structure and open pore mouths of carbon sphere in HPCs-S particles also can be obviously recognized. For HPCs-S, the carbon is distributing over the whole spheres, while the sulfur is mainly distributing over the core area of spheres, by analyzing the elemental mapping (**Figure 7b**). Moreover, linear EDX element distributions of sulfur and carbon along the HPCs-S as shown TEM image in **Figure 7c**. It exhibits the sulfur peak and carbon peak are both through the core area (**Figure 7d**), which indicates that most of extra sulfur is washed away during dissolution process.

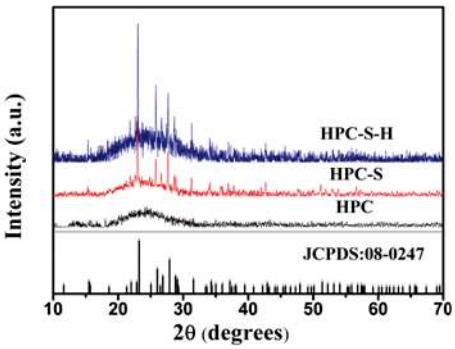

Figure 8. XRD patterns of the as-prepared core-shell HPCs, HPCs-S-H and HPCs-S composite [28].

Figure 8 is XRD patterns of HPCs, HPCs-S-H, and HPCs-S composites. The XRD pattern of HPCs shows a broad peak, which is assigned to the diffraction peak of amorphous carbon [29]. The patterns of HPCs-S-H and HPCs-S exhibit the broad porous carbon peak and sharp peaks for sulfur (JCPDS: 08-0247) [24]. However, it can be seen that the peak intensity of sulfur in the HPCs-S composite is weaker than the HPCs-S-H composite, because the sulfur is dissolving and aggregating on the surface of HPCs-S composite.

3.3. The specific surface areas and pore size distribution curve of core-shell composites

N_2 adsorption-desorption and the corresponding pore size distribution curve of HPCs, HPCs-S-H and HPCs-S composite are shown in **Figure 9**. The HPCs delivered a very high specific surface areas of 957.4 $m^2\ g^{-1}$ and a large total pore volume of 1.459 $cm^3\ g^{-1}$ (p/p_0 = 0.9703) (**Figure 9a, b**). Meanwhile, the average pore size of HPCs sample is 5.98 nm as calculated by the Barrett-Joyner-Halenda (BJH) method. From pore size distribution of the HPCs in **Figure 9b**, the micropores and macropores are 10.6% and 0.9% of the total pore volume, which could effectively hamper the dissolution of sulfur especially for long cycle process [30]. **Table 1** is summarized textural parameters of HPCs, HPCs-S-H, and HPCs-S composites. The mesopore and macropore volume of HPCs-S-H composite are also reduced sharply and micropores is disappear. It indicates that pores of the particles after loading sulfur into HPCs are almost filled with sulfur. And the micropores are fully filled with sulfur. Theoretically, the total pore volume (1.459 $cm^3\ g^{-1}$) of HPCs can contain as much as 75.1 wt% sulfur (s = 2.07 g

cm^{-3}) [31]. Thus the sulfur is not only impregnated in the pores, but also deposited on the external of the spheres. It corresponds to the morphology of HPCs-S-H in **Figure 5**. However, it is shown that the specific surface area and pore volume of HPCs-S composite are increased to 134.3 $m^2\ g^{-1}$ and 0.289 $cm^3\ g^{-1}$ after dissolution treatment (**Figure 9e, f**, and **Table 1**). When used as cathode material for Li-S battery, the void pores existed in the HPCs-S composite is beneficial to tolerate the volumetric expansion of sulfur after lithiation.

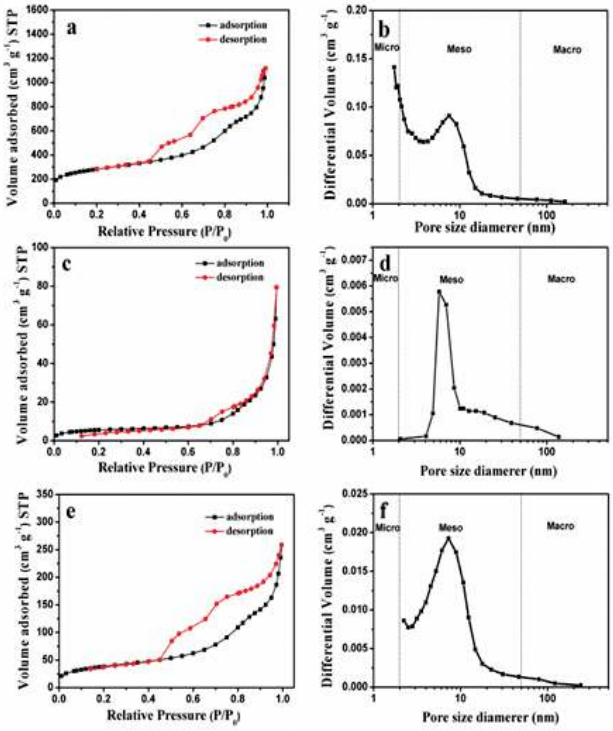

Figure 9. (a) N_2 adsorption-desorption and (b) the corresponding pore size distribution curve of HPCs composite; (c) N_2 adsorption-desorption and (d) the corresponding pore size distribution curve of HPCs-S-H composite; (e) N_2 adsorption-desorption and (f) the corresponding pore size distribution curve of HPCs-S composite [28].

Sample	BET surface area ($m^2\ g^{-1}$)	Total pore volume ($cm^3\ g^{-1}$)	Micropore volume ($cm^3\ g^{-1}$)	Mesopore volume ($cm^3\ g^{-1}$)	Macropore volume ($cm^3\ g^{-1}$)
HPCs	957.4	1.459	0.155	1.291	0.013
HPCs-S-H	18.6	0.067	0	0.0664	0.0006
HPCs-S	134.3	0.289	0	0.2873	0.0017

http://dx.doi.org/10.5772/62439

Table 1. Textural parameters of HPCs, HPCs-S-H and HPCs-S composites.

3.4. The electrochemical performance of core-shell HPCs-S

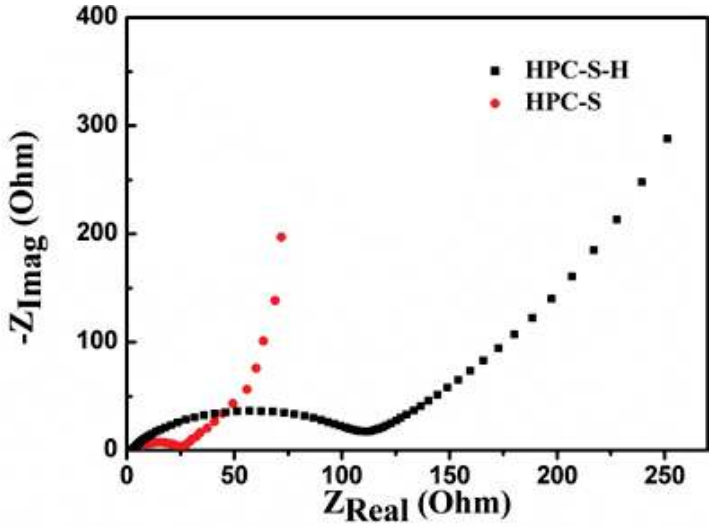

Figure 10. EIS measurements of the MHCs-S-H and MHCs-S electrodes [28].

Figure 10 shows the EIS results of HPCs-S-H and HPsC-S electrodes. In this figure, the resistance of HPCs-S-H electrode is almost four times that of the HPCs-S electrode because of the electrically insulating coating sulfur layer on HPCs-S-H composite isolate the conducting HPCs from the electrolyte, the resistant of HPCs-S-H composite electrode is higher [29, 32]. The CV curves of HPCs-S-H and HPCs-S electrodes in the potential range of 1.5–2.7 V is shown in **Figure 11a**. There are three reductive peaks in the first cathodic process of HPCs-S electrode, due to the multiple reductions of sulfur. The peak at 2.35 V corresponds to the reduction of S_8 to Li_2S_n ($2 \le n \le 8$). The other strong reduction of soluble lithium polysulfides to insoluble lower-order lithium sulfides (Li_2S_2 or Li_2S), because the intense cathodic peak is at 2.02 V. The reduction of high-order polysulfides to medium-order polysulfides, while the small peak is at 2.2 V [33]. There are two oxidation reaction peaks for the HPCs-S electrode. The first peak at 2.35 V is associated with the formation of Li_2S_n ($2 \le n \le 8$). The second peak at 2.45 V is the formation of elemental sulfur [33, 34]. **Figure 11b** is the charge-discharge voltage profiles of the HPCs-S-H and HPCs-S electrodes at 0.2 C (1 C = 1675 mA g^{-1}) in the voltage range of 1.5–2.7 V. The initial discharge capacity and a reversible specific charge capacity of the HPCs-S electrode are 1356 and 1397.9 mAh g^{-1}, which is much higher than the capacities of HPCs-S-H electrode (1080 and 1121.0 mAh g^{-1}). It demonstrates that utilization rate of sulfur for the HPCs-S electrode is much higher. And the electrode of the HPCs-S has sufficient contact with the electrolyte and the conducting material.

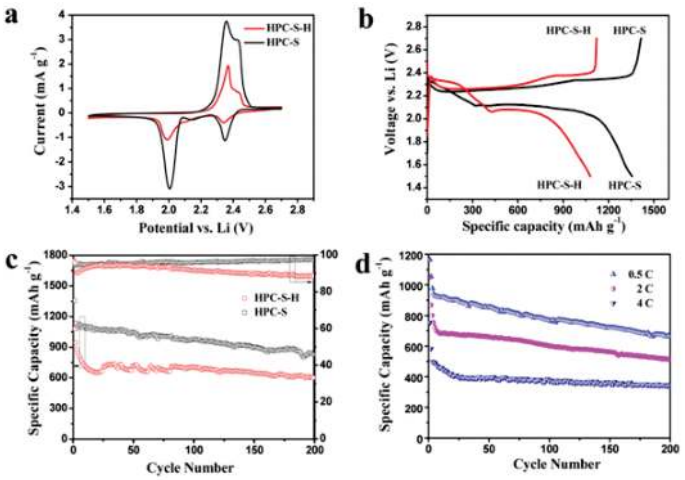

Figure 11. (a) Representative CVs of the HPCs-S-H and HPCs-S electrodes at a scan rate of 0.1 mV s^{-1} between 1.5 and 2.7 V vs. Li/Li^+. (b) Charge-discharge voltage profiles of HPCs-S-H and HPCs-S electrodes for the 1st cycle in the voltage range of 1.5–2.7 V at 0.2 C. (c) Capacity and Coulombic efficiency vs. cycle number of the HPCs-S-H and HPC-S electrodes at 0.2 C. (d) Rate capability of the HPCs-S electrodes [28]

The cycling abilities and the coulombic efficiencies of HPCs-S-H and HPCs-S electrodes at 0.2 C are presented in **Figure 11c**. The specific capacity of HPCs-S-H electrode declined sharply during the first 20 cycles, which is attributed to the dissolution of sulfur on the outer surface of core-shell HPCs [34]. After 200 cycles, the capacity of HPCs-S-H composite was 601.8 mAh g^{-1}. It indicates that the composite suffers a long-term loss of sulfur during cycling. After the exterior sulfur washed away, the reversible capacity of HPCs-S electrode was 830.5 mAh g^{-1} after 200 cycles, which showed much better cycling performance than HPCs-S-H composite. Because there are much more spare void pores and space on the shell of HPCs after dissolution process, it is favorable for electrolyte infiltration and electron transfer [28]. And also, it is beneficial to tolerate the volumetric expansion of sulfur after lithiation [31]. Meanwhile, the coulombic efficiency of HPCs-S electrode maintained about 95.0% during the cycling processes. It is also better than HPCs-S-H electrode. During charge-discharge process, the sulfur is reduced to dissolving polysulfide. Thus, the exterior sulfur layer and the polysulfides escaped from inner pores as the volumetric expansion are readily dissolved in the electrolyte and then lost, as a result, the capacity of HPCs-S-H with a continuous fading on the onward cycles. Furthermore, the soluble polysulfides result in the random precipitation of Li_2S_2 and Li_2S on the electrode, which changes the electrode morphology and increases the resistance of HPCs-S-H electrode [28]. In addition, rate capability behavior of the core-shell HPCs-S composites was detected. The discharge capacities remain 1163.9, 1049.0, and 753.2 mAh g^{-1} at 0.5, 2, and 4 C, separately (**Figure 11d**).

The significant electrochemical performance of the HPCs-S composite can be attributed to the hierarchical porous core-shell structure with high specific surface area and pore volume, which contain the substantial amount of sulfur, and suppress the diffusion of dissolved polysulfides.

http://dx.doi.org/10.5772/62439

And then, the dissolution treatment can prevent sulfur agglomerating on the surface and create void space on the shell of HPCs. It could enhance the transport of lithium ion and infiltration of electrolyte. At last, the outer shell with void pores can avoid effectively the diffusion of dissolved polysulfides and alleviate the stress caused by volume change during the charge-discharge process [28]. The HPCs-S composite with the hierarchical porous core-shell structure maintain the mechanical integrity and chemical stability during the cycling process, because various synergistic effects of the material characteristics and structure design, which could enhance the cycle performance and rate capability of the electrode materials.

4. Synthesized of the sulfur/graphene nanosheets composite

With a few atoms thickness, graphene inherently shows many advantages such as high surface area, excellent electrical conductivity, light weight, good flexibility, and superior mechanical strength, etc. Thus, it can be applied in electronics, engineering materials and is also considered as an ideal substrate for loading active materials like sulfur for electrochemical energy storage.

The application of graphene in Li-S battery is very promising due to its unique 2D structure, high conductivity and superior mechanical flexibility. The S distributed uniformly between the layers of graphene. This structure of carbon atoms is employed as a conductive and absorbing agent for the S cathode materials of rechargeable Li-S battery. Besides, the surface functional groups of graphene can be tuned flexibly to immobilize S/Li_2S_x on the graphene surface during the cycling process. In a recent report by Wang et al., S was melted and coated on the GNS, which shows an improved capacity [35]. Furthermore, a graphene-sulfur composite material was synthesized by synthesizing submicrometer sulfur particles coated with PEG containing surfactants and GNS. The composite showed high specific capacity with relatively good cycling stability as the cathode for Li-S batteries [25].

4.1. The fabrication of the sulfur/graphene nanosheets composite

The graphene oxide (GO) was made using a modified Hummers method [36]. The elemental S is mixed in GO solution at the weight ratio of 1:5, as the mixture designated S/GO solution. The S/GO was ultrasonicated for 30 min to get a uniform suspension and then lyophilized it. The mixture was held at 423 K for 4 h under argon gas protection to allow the melted elemental S to infiltrate into the layers of GNS [37]. Then, the temperature was increased to 573 K and held for 2 h, reduced GO to GNS.

4.2. Morphology and microstructure characterization of the sulfur/graphene nanosheets composite

The SEM images of element S, GNS, and S/GNS composites prepared through reduction are shown in **Figure 12**. In this figure, the morphology of bare S power is microsized particles (**Figure 12a**) and the morphology of graphene is nanosheets (**Figure 12b**), which was reduced by decomposition at 573 K for 4 h under argon gas protection. In **Figure 12c**, the microsized S particles melted and coated uniformly on the GNS sheets was prepared after heat treatment

of S/GO. By the EDS mapping/imaging of the material, it was confirmed that element C and S. And the element S was coated on the GNS sheets uniformly from **Figure 12d, e**, and f.

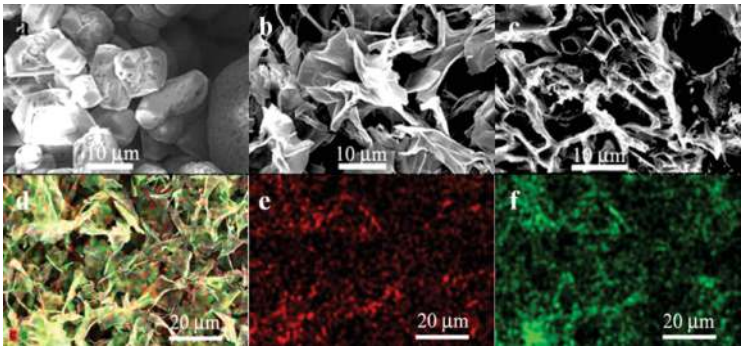

Figure 12. SEM images of (a) elemental S powder, (b) GNS and (c) S/GNS composite. EDS characterization of S/GNS composite. (d) SEM image of GNS coated S particles. (e) EDS mapping of the carbon region shown in (d). (f) EDS mapping of the S region shown in (d) [37].

Figure 13 is the XRD patterns for the S powder and S/GNS composite. The elemental S exhibits several sharp peaks, indicating its good crystal state. However, the characteristic peaks of crystal S in the S/GNS composite with a low S content are not detectable. It demonstrate that S becomes amorphous and homogeneously distributed in the composite.

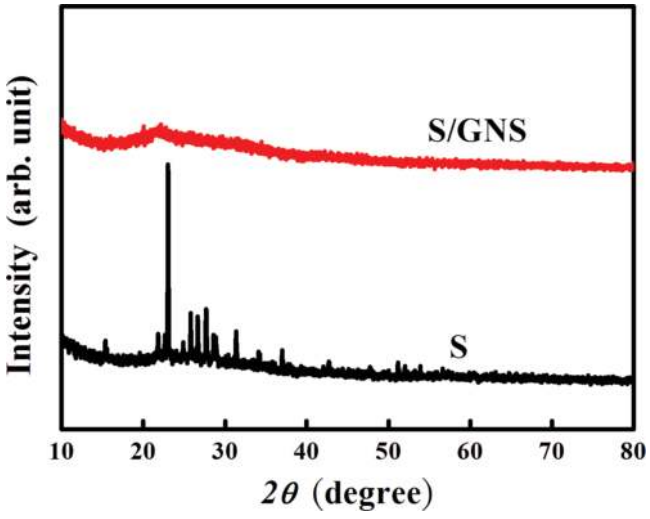

Figure 13. XRD patterns of elemental S and S/GNS composite [37].

http://dx.doi.org/10.5772/62439

4.3. The electrochemical performance of the sulfur/graphene nanosheets composite

Figure 14a shows the discharge curves of the S and S/GNS composite, which represent a typical characterization of Li-S batteries. The upper plateau shows the change from elemental S to the higher order Li polysulfides (Li_2S_n, $8 > n > 2$), and the lower plateau indicates the reduction of the higher order Li polysulfides to lower order Li sulfides (Li_2S_2, Li_2S). From this figure, the initial discharge specific capacity of S/GNS cathode is about 1598 mAh g^{-1}. In contrast, the initial discharge-specific capacity of the S cathode is about 1094 mAh g^{-1}. The cycling performances of the pure S and S/GNS composite electrode at the constant current density of 160 mAh g^{-1} S is shown in **Figure 14b**. The discharge specific capacity of the S/GNS composite electrode decreases from initial 1598 to 670 mAh g^{-1} after 80 cycles. Compared to the pure S electrode, the initial capacity and the cycling stability of the S/GNS electrode are both improved.

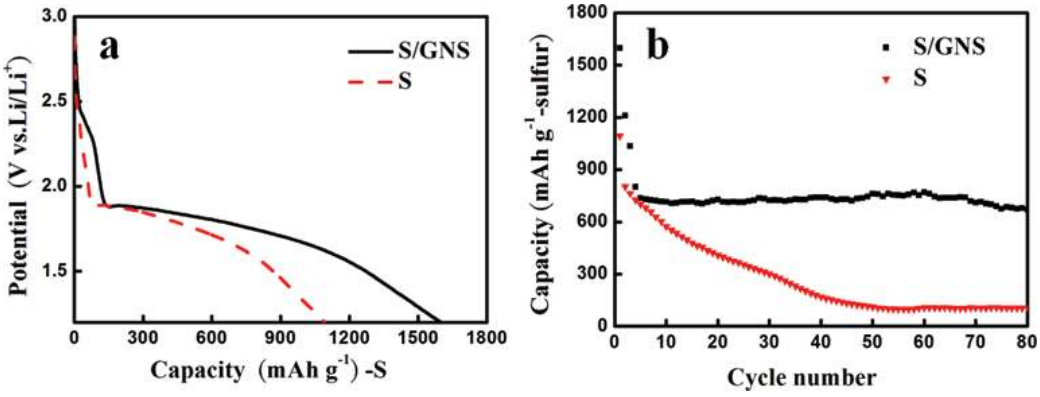

Figure 14. First discharge curves of the S and S/GNS composite electrodes and cycle performance for S and S/GNS composite electrodes [37].

Furthermore, EIS of the differences two electrodes is investigated in Nyquist profiles (**Figure 15**). It indicates that all the Nyquist plots of cathodes are composed by a semicircle at high frequencies relating to the contact resistance and charge transfer resistance, and a short inclined line in low-frequency regions due to the ion diffusion within the cathode [37]. It can be inferred that GNS can provide a better electron and ionic conductivity network, because the semicircle in S/GNS electrode is much smaller than the S electrode.

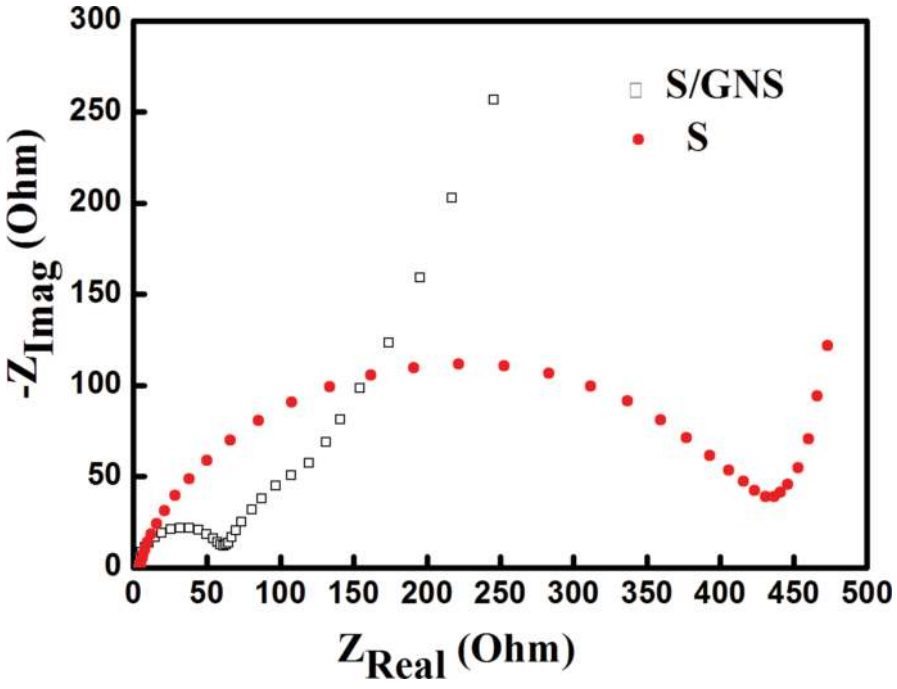

Figure 15. Impedance plots for electrodes of S and S-GNS composite [37].

5. Synthesized of a sulfur@rGO composite with a saccule-like structure

In contrast to graphene, GO is a compound of carbon, oxygen, and hydrogen in variable ratios and is rich in epoxide, carbonyl, hydroxyl, phenol, and organosulfate functional groups, whose structure and properties depend on the particular synthesis method and degree of oxidation [38]. The micro-sized sulfur nanoparticles enveloped by the rGO was synthesized by a scalable solution-based oxidation process. It had been achieved a high loading amount of sulfur (87%) embedded into the rGO matrix [39]. The synthesized GO is hydrophilic and easily dispersed in water, making it suitable for the synthesis of sulfur-graphene composites. In general, graphene-based materials are less expensive to produce than some other carbon nanomaterials such as carbon nanotubes, which is advantageous when they are applied as raw materials for the synthesis of graphene-based composite materials.

It has been reported that sulfur-graphene composite was synthesized by using several methods [40]. However, the 2D structure is not effective in containing the polysulfides, although the graphene could improve the conductivity of sulfur. In the recent reports, the GO-sulfur composite showed high specific capacity with relatively good cycling stability as the cathode

for Li-S cells, which showed high specific capacity with relatively good cycling stability as the cathode for Li-S cells [41].

5.1. The schematic representation of sulfur@rGO composite with a saccule-like structure

The detailed synthetic procedures are shown in **Figure 16**. First, graphite oxide (GO) synthesized by a modified Hummers method is dispersed with water to form a homogeneous suspension (water-phase) under ultrasonic condition. Then the oil-phase containing sulfur in carbon disulfide (CS_2) is dropwise added into GO solution under ultrasonication. Followed by completely evaporation of CS_2 from the mixture, hydrazine hydrate ($N_2H_4{\cdot}H_2O$) is then added to reduce GO to rGO. After stirring for 12 h at room temperature, the S@rGO composite is collected by consecutive centrifugation and water-washing cycles as well as lyophilization.

Figure 16. Schematic of synthesis steps for S@rGO composite [42].

5.2. Morphology and microstructure characterization of sulfur@rGO composite

The microstructures of the as-synthesized sample are characterized by SEM. The dimension of the composite particles before reduction is ca. 1 μm (**Figure 17a**). Meanwhile, the image shows GO sheets coat around the particles, indicating the feasibility of our strategy in preparing encapsulated structure using O/W system. Interestingly, after reduction with $N_2H_4{\cdot}H_2O$, the size and surface morphology of the composite particles can be kept almost unchanged (**Figure 17c**). The morphology and structure of the interior sulfur were analyzed by TEM in **Figure 17d**. Unexpectedly, the interior sulfur encapsulated by rGO is composed of many smaller particles with the size ranging from 10 to 100 nm. When the oil droplets of CS_2 containing sulfur are first split into smaller droplets and surrounded by GO sheets under ultrasonic condition. Then, due to the volatile nature of CS_2, it gradually evaporated from the O/W system accompanied by forming the saccule-like structure and making the dissolving sulfur recrystallize into smaller particles [42]. It should be noted that the obtained saccule-like structure has enough space to accommodate volumetric expansion of sulfur during charge-discharge process.

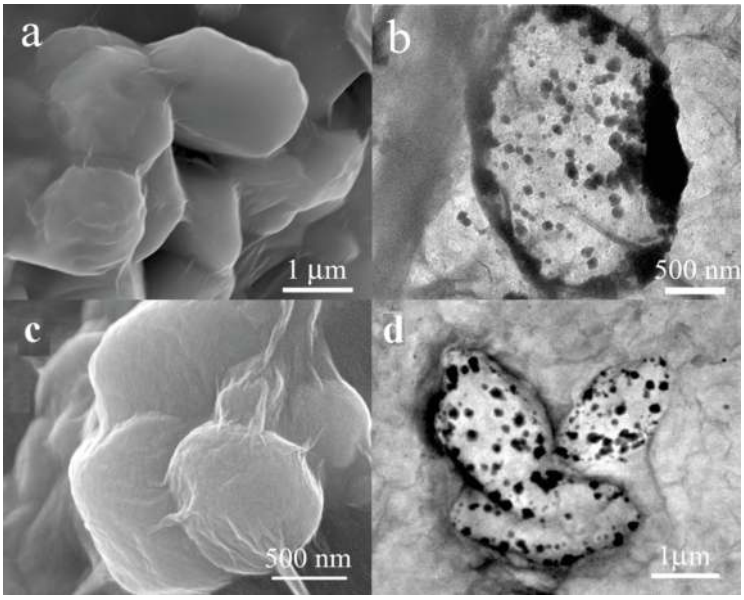

Figure 17. SEM and TEM images of S@GO and S@rGO composite [42].

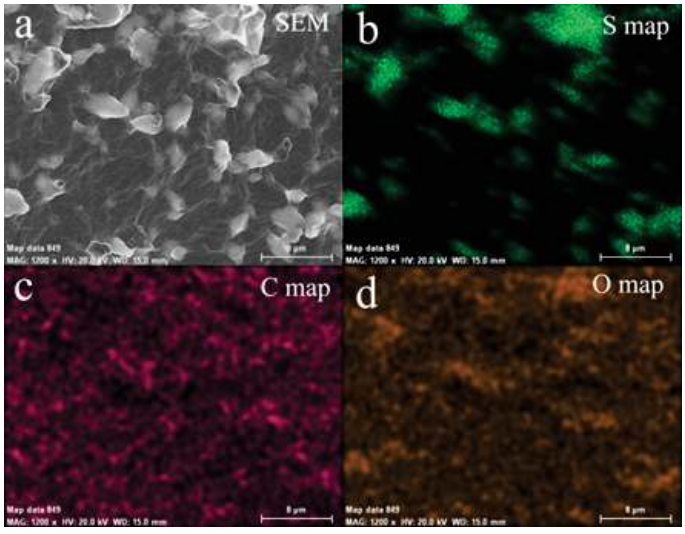

Figure 18. EDS characterization of S@rGO composite. (a) SEM image of rGO-coated sulfur particles. (b) EDS sulfur mapping of the region shown in (a). (c) EDS carbon mapping of the region shown in (a). (d) EDS oxygen sulfur mapping of the region shown in (a) [42].

http://dx.doi.org/10.5772/62439

In **Figure 18**, the structure and composition of the S@GO composite was verified by EDS mapping of the material. It is shown that sulfur is encapsulated by GO in the saccule-like structure. The relative change in the ratio of D to G peak intensity before and after the reduction in the Raman spectrum confirms the reduction of GO (**Figure 19a**) [28]. The XRD analyses are also conducted on the obtained S@rGO composite and elemental sulfur (**Figure 19b**). The reflections of the elemental sulfur showed two prominent peaks at 2θ = 23° and 28° corresponding to an F3d orthorhombic structure [43, 44]. As shown, the characteristic peaks in XRD pattern of the elemental sulfur and S@rGO composite remain the same, further indicating the existence of sulfur in the saccule-like structure. And then, the content of sulfur in the S@rGO is as high as 65 wt% by elementary analysis.

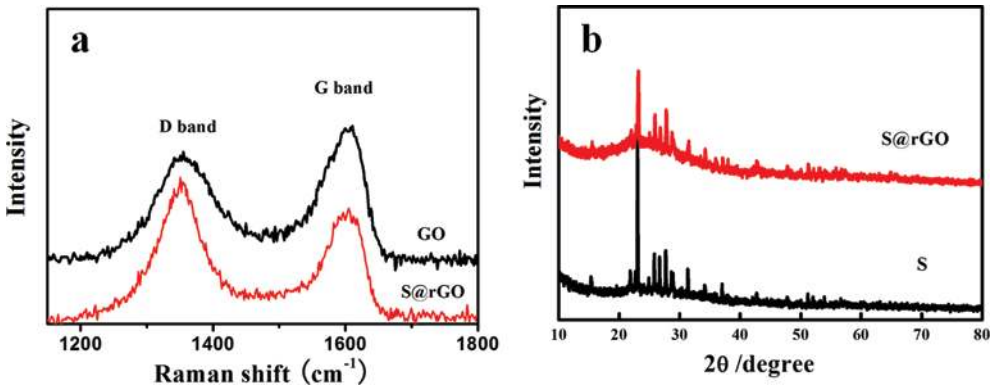

Figure 19. (a) Raman spectra of the GO solution and S@rGO composite, (b) XRD patterns of the element S and S@rGO composite [42].

5.3. The electrochemical performance of sulfur@rGO composite with a saccule-like structure

Figure 20a shows the first cycle charge and discharge curves of the sulfur@rGO composite at different high rates. The discharge capacity of composite is 724.5 mA h g^{-1} at a current rate of 1 C (1 C = 1675 mA g^{-1}). And also, the discharge capacity remains as high as 715.6, 708.6, and 697.5 mA h g^{-1} at 2, 3, and 4 C, respectively, which is much better than the S-rGO cathode. **Figure 21** is CV profile for indicating the electrochemical reactions of the composite cathode, which suggests a two-step reduction of sulfur. However, there is only one intensive oxidation peak at about 2.5 V, in the subsequent anodic scan, which indicates the conversion of Li_2S and polysulfides into elemental S.

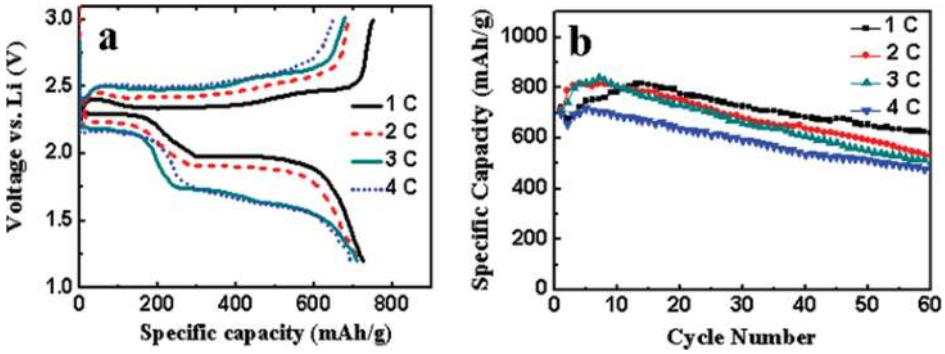

Figure 20. (a) First cycle charge/discharge voltage profiles of the S@rGO cathodes at various C rates. (b) Cycle performance of the S@rGO cathodes at various C rates [42].

The cycling performance of the S@rGO composite for the Li-S cell is shown in **Figure 20b**. The discharge capacity increased gradually with increasing cycle number during initial several cycles, because the S@rGO composite in the cathodes are incompletely soaking and penetrating with the electrolyte. After the 60th cycle, the cathode holds the reversible discharge specific capacity of 621.9 mA h g^{-1}, at a rate of 1 C. At the high rates of 2, 3, and 4 C, the capacities can remain 530.8, 505.8, and 478.7 mA h g^{-1}, respectively, and the 60th charge/discharge profiles are also shown the good performance of the cells.

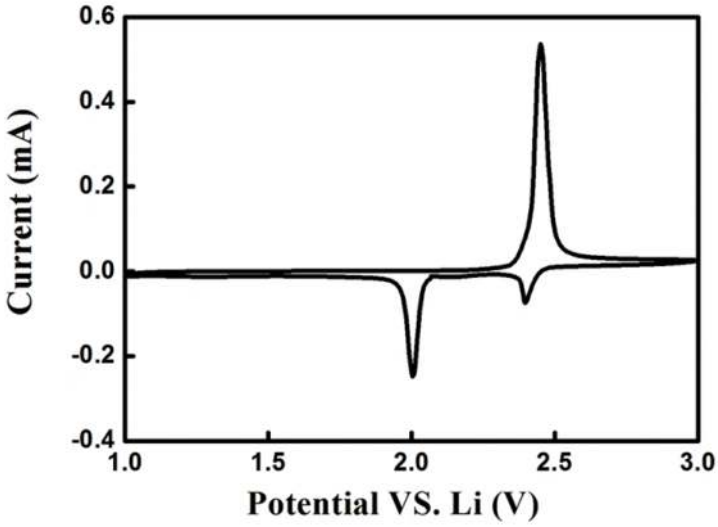

Figure 21. Cycling voltammetry curve of the first cycle at scan rate of 0.1 mV s^{-1} [42].

So, the good cycling stability of the cathode at high rates is owing to the excellent flexibility and mechanical strength of graphene, meanwhile, the unique saccule-like structure of the composite could provide enough space to accommodate stress and sulfur volumetric expansion during charge-discharge process [42]. Although the cycling stability and rate capacity of sulfur@rGO composite have been improved obviously, the problem of polysulfides dissolution has not been solved completely, leading to some capacity loss in the cycling process. So, the conductive polymer has been coated onto the surface of sulfur particles to improve the electronic conductivity.

6. Synthesized of the C-S@PANI composite with polymer spherical network structured

Focused on creating fine structures, the polymer/S-C composites utilize interactions between lithium ions in solution and functional group uniformly distributed along the chain backbone of a polymer precursor. The novelty structure could control the distribution of lithium sulfide in the host material similar to vulcanization methods [44]. In addition, some additives, especially $LiNO_3$, could enhance the coulombic efficiency via self-sacrifice [45]. Among the family of conductive polymers, PANI is attractive because of its associated electrical, electrochemical, optical properties and free volume, coupled with its excellent environmental stability [46, 47]. Cui's group also reported a nano-structured polymer-wrapped hollow sulfur nanospheres-based composite with enhanced specific capacity and cycling performance [48]. This approach is coating a conductive polymer onto the surface of sulfur particles to improve the electronic conductivity of cathodes and prevent the dissolution of polysulfides [42, 49]. These approaches improve the utilization of sulfur and cycle stability to different extents.

6.1. The schematic representation of the C-S@PANI composite with PSN

A new scheme is proposed to prepare composites based on lithium sulfide uniformly dispersed in Polymer Spherical Network by the in situ synthesis technique. The C-S@PANI composite with conductive PSN has been synthesized by a grafting method. **Figure 22** shows a schematic illustration of the synthesis process. Firstly, the suspension of oxidized carbon black (CBO) is prepared by dispersing stoichiometries Acetylene black (AC) in concentrated nitric acid (HNO_3). Secondly, hydrochloric acid solution (HCl) is prepared and mixed with CBO, adding aniline (ANi) under ice cooling (0–4°C) with magnetic stirring. Then the initiator (the molar amount of ammonium persulfate (APS) and ferric chloride ($FeCl_3$) is 1:0 to 1:1) is added dropwise while stirring the mixed suspension of CBO/ANi (speed < 0.5 mL/min). The solution is stirred, sealed, and reacted for t_1 (18 h) at 0–4°C, t_2 (24 h) at room temperature (20–30°C), ultrasonicated for 10 min, washed with acetone and deionized water, ultrasonicate after each wash and centrifuge to obtain the conductive polymer (CBO-PANI). And last, the sulfur of composite materials is filled by the liquid phase deposition method, first mixture (CBO-PANI) is added into HCl solution and stirred for 5 min [47]. Sodium thiosulfate ($Na_2S_2O_3{\cdot}5H_2O$) (rate v_2 < 1 mL/min) is added dropwise with magnetic stirring into the conductive frame (CBO-

PANI). After stirring, the solution is heated at 155°C for 18 h. Washed with deionized water and alcohol, with ultrasonication after each wash, the composite (C-S@PANI) is obtained through centrifugation [47].

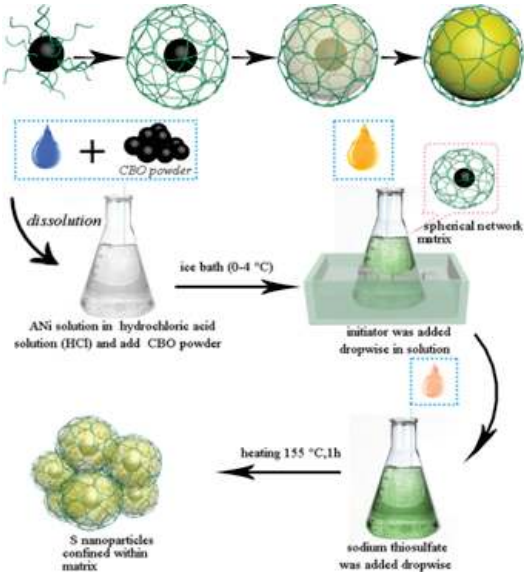

Figure 22. The design of PSN matrix (C-S@PANI composite) as the cathode materials for lithium-sulfur batteries (Green: PANI, yellow: sulfur, black: acetylene black), and schematic illustration of the synthesis process [47].

6.2. Morphology and microstructure characterization of the C-S@PANI composite with PSN

During the co-heating process, the molten sulfur can penetrate into the PANI spherical network. At the same time, the network shows strong absorption ability to receive elemental sulfur. **Figure 23** is the morphology of C-S@PANI composite. The typical matrix structure of the C-S@PANI composite with C-S particles reunited to form spherical particle with sizes of 80–100 nm is showed clearly in this figure. The whole particle congeries completely are enclosed and pinned by the PANI network matrix of nearly 20 nm in thickness. As shown in **Figure 23d**, the sulfur and carbon can maintain uniform distribution on a single spherical particle. It is also indicated that sulfur is encapsulated within the PANI matrix uniformly after heating. From morphology images of C-S@PANI composite, there are many pores, which can absorb polysulfide when the PANI layer connects to the C-S particles to form a micro-reactor. Furthermore, the pores provide channels for electrolyte infiltration and ion diffusion. At the same time, the pores provide much more spaces for volume expansion produced by the sulfur discharge products. On the other hand, chemical bond generated due to the chemical effect, the interaction between the functional group of conductive polymer surface, and the reactions products of the polysulfide [50], resulting in excellent sulfur wrapped.

http://dx.doi.org/10.5772/62439

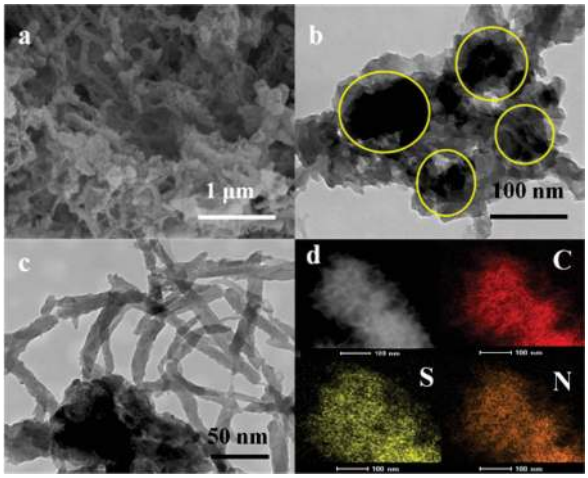

Figure 23. (a) SEM images and (b), (c) TEM images of C-S@PANI composites (d) EDX elemental mappings of carbon, sulfur and nitrogen [47].

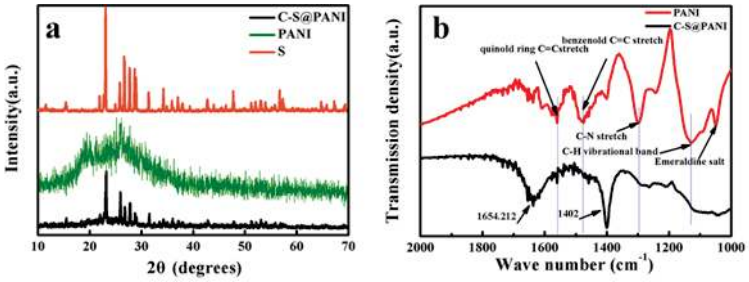

Figure 24. (a) XRD patterns of sublimed S, PANI and C-S@PANI composite 40% of sulfur, (b) FTIR spectra of the PANI and C-S@PANI composite [47].

The XRD analyses and FTIR spectra of the PANI and C-S@PANI composite after heat treatment are shown in **Figure 24**. In the XRD patterns, the C-S@PANI composite exhibits significantly lower peak intensities than the sulfur. It indicates the amorphous nature of the sulfur within the composite. FTIR measurement illustrates the presence of chemical bonds and functional groups between with PANI matrix and sulfur, in **Figure 24b**. The C=C stretching vibration at 1497 cm^{-1}, assigned to benzenoid rings shifts to lower wave numbers, which could be coming from the substitution of H atoms on benzenoid rings by S atoms [47]. The C-N stretching vibrational bands at 1298.4 cm^{-1} and the C-H vibrational band in the vicinity of 1128.7 cm^{-1} weakens significantly, further confirming the replacement of H atoms on aromatic rings by S atoms [47]. C-S@PANI composite with PSN provides strong physical and chemical confinement to the elemental sulfur and the resident polysulfide.

6.3. The electrochemical performance of the C-S@PANI composite with PSN

Figure 25 is the electrochemical performances of the C-S@PANI composite with PSN structure by galvanostatic charge/discharge cycling. In **Figure 26a**, there are two voltage plateaus at 2.3 and 2.0 V at 0.1 C (according to the theoretical capacity of sulfur is calculated 1 C=1672 mAh/g). The elemental sulfur capacity is calculated by subtracting the amount of carbon black and polyaniline from the (PSN/S). The high voltage plateau corresponds to the long polysulfide chains being produced during the first reduction step (2.4–2.2 V), such as S_8^{2-} and S_6^{2-}, as well as S_4^{2-} being produced during the second reduction step (2.15–2.1 V) [49]. The low-voltage plateau is attributed to the gradual decrease of the polysulfide chain lengths. Finally, short polysulfide species, such as S_3^{2-}, S_2^{2-}, and S^{2-}, are produced at the end of the reduction process [51]. The electrode exhibits a discharge and charge capacity of 608 and 628 mA h g^{-1} at 0.1 C for the first cycle. And the discharge and charge capacity increased to 1238 and 1453 mA h g^{-1}, after 20 cycles in **Figure 26a**. **Figure 26b** is cycling performance of C-S@PANI composites, which shows that C-S@PANI composite with PSN structure remain relatively stable at a value as high as 948 mA h g^{-1} after 200 cycles at 0.1 C. Meanwhile, the specific capacity of composite are 758 and 743 mA h g^{-1} after 200 cycles at 0.2 C and 0.5 C, respectively. In addition, as seen in **Figure 26c**, the discharge capacity of the composite cathode returns to 1012 mA h g^{-1} from 727 mA h g^{-1}, when the rate decreases from 0.5 C to 0.1 C. From the EIS of the composite electrode after 50 cycles (**Figure 26d**), there are wo depressed semicircles in the middle and high frequency region and an oblique line in low-frequency region. The semicircle from high to medium frequency represents the SEI layer resistance, which was adopted to protect the lithium anode and improve coulombic efficiency. The intermediate frequency semicircle represents charge transfer resistance between the electrolyte and cathode electrode, and the oblique line represents diffusion impedance [47].

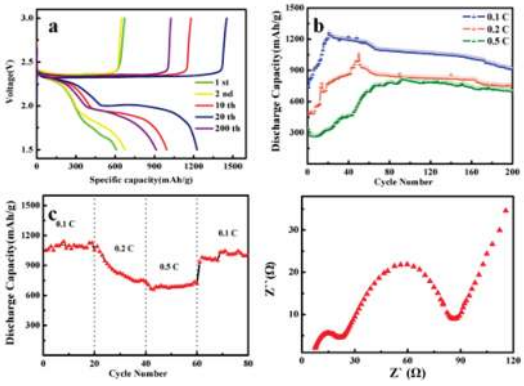

Figure 25. (a) Charge-discharge profile for the C-S@PANI composite at 0.1 C between 0.1 and 3.0 V (vs. Li/Li^+) at room temperature, (b) cycle performance of the C-S@PANI composite at 0.1, 0.2, and 0.5 C, respectively, (c) rate performance of C-S@PANI composite. (d) Electrochemical impedance spectra of the composite electrode after 50 cycles [47].

http://dx.doi.org/10.5772/62439

6.4. The charge-discharge mechanism of the C-S@PANI composite with PSN as cathode for high performance lithium-sulfur batteries

There are multiple reactions in the charge-discharge reaction of a lithium-sulfur battery. Sulphur can react with metallic lithium to form Li_2S with a large negative free energy change, which can be harnessed in a battery with a two-electron reaction [47]. As the redox reaction, sulfur entirely dissolves into the liquid electrolyte in the form of Li_2S_8 with S_8 ring as the initial form. The color of catholyte changed from red to green with decreasing chain length of polysulfides [52]. The final product is insoluble Li_2S_2 or Li_2S, which is deposited on the electrode surface, blocking further reaction. This process of inclusion complex disproportionation results in the "shuttle effect" [51]. The total reaction is as follows: $S_8 + 16Li \rightarrow 8Li_2S$. The PSN provides access to Li^+ ingress/egress for conversion of Li_2S to Li_2S_x (as illustrated in **Figure 26**).

The higher specific capacity and excellent cycle stability are achieved simultaneously, which can be attributed to the special microstructure of the C-S@PANI composite. At first, the C-S core-shell composites coated by the conductive PANI form a three-dimensional conducting network in **Figure 26a**. It is beneficial for enhancement of the rate capability of sulfur cathode, because the utilization of the active mass and dual conduction of Li^+ and electrons. Secondly, the much more mass of sulfur could be encapsulated into the PANI hollow spherical network in order to generate the S-C bonds act as the bridge between the PANI and sulfur or polysulfides, during heating treatment. The structure of hyperbranched, high aspect ratio, and multiple cross junctions can inhibit effectively the dissolution and migration of polysulfides into the electrolyte, thus effectively enhancing the cycling stability and the coulombic efficiency of the electrode at high current rates [47, 53]. In addition, the PANI hollow network could supply sufficient space to buffer the large volume expansion of sulfur during the charge-discharge process (**Figure 26b**). Thus, as the cathode material of C-S@PANI composite with PSN structure, the superior specific capacity, rate stability, and excellent cycling performance of the lithium sulfur battery should be improved.

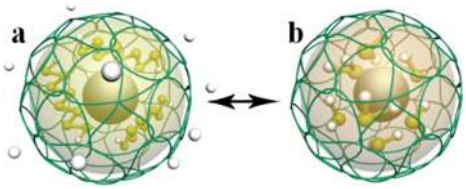

Figure 26. Li_2S (orange color) trapping within the PANI framework during lithiation/delithiation (yellow and gray are the sulfur and lithium) [47].

7. Conclusions

In this chapter, new kinds of cathode materials for lithium sulfur batteries have been designed and synthesized. Generally, sulfur cathodes have diversified through microstructure design-

ing with various materials, including core-shell HPC spheres, graphene, GOs, polymers and their hybrids, which should effectively inhibit the dissolution and migration of polysulfides into the electrolyte, and volume expansion during discharge. In addition, as cathode material for Li-S secondary batteries, the as-prepared new kind cathodes which improve the cycling stability and the coulombic efficiency of the electrode at different current rates and temperature, exert outstanding electrochemical features. So, the future work in the electrolyte area for Li-S batteries should focus on inhibiting the dissolution of polysulfides in electrolytes while optimizing their ionic and charge conductivity without compromising properties during prolonged electrochemical cycles.

Acknowledgements

This work was supported by the State Scholarship Fund of China Scholarship Council (grant no. 201408220025), Science Foundation of Jilin Education Department (grant no. 2015118), and the Special Funds of Changchun University of Technology.

Author details

Lianfeng Duan[1*], Feifei Zhang[2] and Limin Wang[2]

*Address all correspondence to: duanlf@ccut.edu.cn

1 Key Laboratory of Advanced Structural Materials, Ministry of Education, Department of Materials Science and Engineering, Changchun University of Technology, Changchun, China

2 State Key Laboratory of Rare Earth Resource Utilization, Changchun Institute of Applied Chemistry, Chinese Academy of Sciences, Changchun, China

References

[1] A. Manthiram, Y. Fu, S. H. Chung, C. Zu, Y. S. Su. Rechargeable lithium-sulfur batteries. Chem Rev. 2014;114:11751–11787.

[2] G. Xu, B. Ding, J. Pan, P. Nie, L. Shen, X. Zhang. High performance lithium-sulfur batteries: advances and challenges. J Mater Chem A 2014;2:12662–12669.

[3] S. Zhang, K. Ueno, K. Dokko, M. Watanabe. Recent advances in electrolytes for lithium-sulfur batteries. Adv. Energy Mater. 2015;5:15–43.

[4] R. Wu, D. P. Wang, X. Rui, B. Liu, K. Zhou, A. W. Law, Q. Yan, J. Wei, Z. Chen. In-situ formation of hollow hybrids composed of cobalt sulfides embedded within porous

carbon polyhedra/carbon nanotubes for high-performance lithium-ion batteries. Adv Mater. 2015;27:3038–3044.

[5] M. A. Pope, I. A. Aksay. Structural design of cathodes for Li-S batteries. Adv. Energy Mater. 2015;5:1500124–1500146.

[6] R. Chen, T. Zhao, F. Wu. From a historic review to horizons beyond: lithium-sulphur batteries run on the wheels. Chem Commun. 2015;51:18–33.

[7] D. Herbert, J. Ulam. Electric dry cells and storage batteries. US3043896, 1962.

[8] J. R. Birk, R. K. Steunenberg. Chemical investigations of lithium-sulfur cells advances in chemistry. Am Chem Soc. 1975;140:186–202.

[9] H. Yamin, E. Peled. Electrochemistry of a nonaqueous lithium/sulfur cell. J Power Sources 1983;9:281–287.

[10] H. Yamin, J. Penciner, A. Gorenshtain, M. Elam, E. Peled. The electrochemical behavior of polysulfides in tetrahydrofuran. J Power Sources 1985;14:129–134.

[11] Y. F. A. Manthiram, Y. S. Su. Challenges and prospects of lithium-sulfur. Accounts Chem Res. 2012;46:1125–1134.

[12] R. Xu, J. Lu, K. Amine. Progress in mechanistic understanding and characterization techniques of Li-S batteries. Adv Energy Mater. 2015;5:1500430.

[13] D. W. Wang, Q. Zeng, G. Zhou, L. Yin, F. Li, H. M. Cheng, I. R. Gentle, G. Q. M. Lu. Carbon-sulfur composites for Li-S batteries: status and prospects. J Mater Chem A 2013;1:9382–9394.

[14] M. Barghamadi, A. S. Best, A. I. Bhatt, A. F. Hollenkamp, M. Musameh, R. J. Rees, T. Rüther. Lithium-sulfur batteries the solution is in the electrolyte, but is the electrolyte a solution? Energy Environ Sci. 2014;7:3902–3920.

[15] Y. Yang, G. Zheng, Y. Cui. Nanostructured sulfur cathodes. Chem Soc Rev. 2013;42:3018–3032.

[16] S. Chen, X. Huang, H. Liu, B. Sun, W. Yeoh, K. Li, J. Zhang, G. Wang. 3D Hyperbranched hollow carbon nanorod architectures for high-performance lithium-sulfur batteries. Adv Energy Mater. 2014;4:1301761–1301770.

[17] Y. Dong, S. Liu, Z. Wang, Y. Liu, Z. Zhao, J. Qiu. Sulfur-infiltrated graphene-backboned mesoporous carbon nanosheets with a conductive polymer coating for long-life lithium-sulfur batteries. Nanoscale 2015;7:7569–7573.

[18] H. S. Ryu, H. J. Ahna, K. W. Kim, J. H. Ahnb, J. Y. Lee. Discharge process of Li/PVdF/S cells at room temperature. J Power Sources 2006;153:360–364.

[19] H. Kim, H. D. Lim, J. Kim, K. Kang. Graphene for advanced Li/S and Li/air batteries. J Mater Chem A 2014;2:33–47.

[20] L. F. Nazar, M. Cuisinier, Q. Pang. Lithium-sulfur batteries. MRS Bull. 2014;39:436–442.

[21] Y. V. Mikhaylik, J. R. Akridge. Polysulfide shuttle study in the Li/S battery system. J Electrochem Soc. 2004;151:A1969–A1976.

[22] L. Suo, Y. S. Hu, H. Li, M. Armand, L. Chen. A new class of solvent-in-salt electrolyte for high-energy rechargeable metallic lithium batteries. Nat Commun. 2013;4:1481–1489.

[23] J. L. Wang, J. Yang, J. Y. Xie, N. X. Xu. A novel conductive polymer-sulfur composite cathode material for rechargeable lithium batteries. Adv Mater. 2002;14:963–965.

[24] B. Wang, Y. F. Wen, D. L. Ye, H. Yu, B. Sun, G. X. Wang, D. H. Jurcakova, L. Z. Wang. Dual protection of sulfur by carbon nanospheres and graphene sheets for lithium-sulfur batteries. Chem Eur J. 2014;20:5224–5230.

[25] H. L. Wang, Y. Yang, Y. Y. Liang, J. T. Robinson, Y. G. Li, A. Jackson, Y. Cui, H. J. Dai. Graphene-wrapped sulfur particles as a rechargeable lithium-sulfur battery cathode material with high capacity and cycling stability. Nano Lett. 2011;11:2644–2647.

[26] C. F. Zhang, H. B. Wu, C. Z. Yuan, Z. P. Guo, X. W. Lou. Confining sulfur in double-shelled hollow carbon spheres for lithium–sulfur batteries. Angew Chem. 2012;124:9730–9733.

[27] N. Jayaprakash, J. Shen, S. S. Moganty, A. Corona, L. A. Archer. Porous hollow carbon@sulfur composites for high-power lithium-sulfur batteries. Angew Chem. 2011;123:6026–6030.

[28] F. F. Zhang, G. Huang, X. X. Wang, Y. L. Qin, X. C. Du, D. M. Yin, F. Liang, L. M. Wang. Sulfur-impregnated core-shell hierarchical porous carbon for lithium-sulfur batteries. Chem Eur J. 2014;20:1–8.

[29] B. Zhang, X. Qin, G. R. Li, X. P. Gao. Enhancement of long stability of sulfur cathode by encapsulating sulfurinto micropores of carbon spheres. Energy Environ Sci. 2010;3:1531–1537.

[30] C. Tang, Q. Zhang, M. Q. Zhao, J. Q. Huang, X. B. Cheng, G. L. Tian, H. J. Peng, F. Wei. Nitrogen-doped aligned carbon nanotube/graphene sandwiches: facile catalytic growth on bifunctional natural catalysts and their applications as scaffolds for high-rate lithium-sulfur batteries. Adv Mater. 2014;26:6100–6105.

[31] G. He, S. Evers, X. Liang, M. Cuisinier, A. Garsuch, L. F. Nazar. Tailoring porosity in carbon nanospheres for lithium-sulfur battery cathodes. ACS Nano. 2013;7:10920–10930.

[32] G. M. Zhou, D. W. Wang, F. Li, P. X. Hou, L. C. Yin, C. Liu, G. Q. Lu, I. R. Gentle, H. M. Cheng. A flexible nanostructured sulphur-carbon nanotube cathode with high rate performance for Li-S batteries. Energy Environ Sci. 2012;5:8901–8906.

[33] J. C. Guo, Y. H. Xu, C. S. Wang. Sulfur-impregnated disordered carbon nanotubes cathode for lithium-sulfur batteries. Nano Lett. 2011;11:4288–4294.

[34] C. Lai, X. P. Gao, B. Zhang, T. Y. Yan, Z. Zhou. Synthesis and electrochemical performance of sulfur/highly porous carbon composites. J Phys Chem C 2009;113:4712–4716.

[35] J. Z. Wang, L. Lu, M. Choucair, J. A. Stride, X. Xu, H. K. Liu. Sulfur-graphene composite for rechargeable lithium batteries. J Power Sources 2011;196:7030–7034.

[36] D. C. Marcano, D. V. Kosynkin, J. M. Berlin, A. Sinitskii, Z. Sun, A. Slesarev, L. B. Alemany, W. Lu, J. M. Tour. Improved synthesis of graphene oxide. ACS Nano. 2010;4:4806–4814.

[37] F. F. Zhang, Y. H. Dong, Y. Huang, G. Huang, X. B. Zhang, L. M. Wang. Preparation and performance of a sulfur/graphene composite for rechargeable lithium-sulfur battery. J Phys Conf Ser. 2012;339:012003–012008.

[38] S. Evers, L. F. Nazar. Graphene-enveloped sulfur in a one pot reaction: a cathode with good coulombic efficiency and high practical sulfur content. Chem Commun. 2012;48:1233–1235.

[39] A. K. Geim, K. S. Novoselov. The rise of graphene. Nat Mater. 2007;6:183–191.

[40] L. Ji, M. Rao, H. I. Zheng, L. Zhang, Y. Li, W. Duan, J. Guo, E. J. Cairns, Y. Zhang. Graphene oxide as a sulfur immobilizer in high performance lithium/sulfur cells. J Am Chem Soc. 2011;133:18522–18525.

[41] X. Ji, K. Lee, L. Nazar. A highly ordered nanostructured carbon-sulphur cathode for lithium-sulphur batteries. Nat Mater. 2009;8:500–506.

[42] F. F. Zhang, X. B. Zhang, Y. H. Dong, L. M. Wang. Facile and effective synthesis of reduced graphene oxide encapsulated sulfur via oil/water system for high performance lithium sulfur cells. J Mater Chem. 2012;22:11452–11454.

[43] J. H. Shin, E. J. Cairns. N-Methyl-(n-butyl)pyrrolidinium bis(trifluoromethanesulfonyl)imide-LiTFSI-poly(ethylene glycol) dimethyl ether mixture as a Li/S cell electrolyte. J Power Sources 2008;177:537–545.

[44] J. Wang, Y. S. He, J. Yang. Sulfur-based composite cathode materials for high-energy rechargeable lithium batteries. Adv Mater. 2014;3:569–572.

[45] S. S. Zhang, J. A. Read. A new direction for the performance improvement of rechargeable lithium/sulfur batteries. J Power Sources 2012;200:77–82.

[46] J. X. Huang, S. Virji, B. H. Weiller, R. B. Kaner. Polyaniline nanofibers: facile synthesis and chemical sensors. J. Am. Chem. Soc. 2003;125:314–315.

[47] J. K. Wang, K. Q. Yue, X. D. Zhu, K. L. Wang, L. F. Duan. C-S@PANI composite with a polymer spherical network structure for high performance lithium-sulfur batteries. Phys Chem Chem Phys. 2016;18:261–266.

[48] W. Li, Q. Zhang, G. Zheng, Z. W. Seh, H. Yao, Y. Cui. Understanding the role of different conductive polymers in improving the nanostructured sulfur cathode performance. Nano Lett. 2013;13:5534–5540.

[49] L. F. Xiao, Y. L. Cao, J. Xiao, B. Schwenzer, M. H. Engelhard, L. V. Saraf, Z. M. Nie, G. J. Exarhos, J. Liu. A soft approach to encapsulate sulfur: polyaniline nanotubes for lithium-sulfur batteries with long cycle life. Adv Mater. 2012;24:1176–1181.

[50] W. Zhou, Y. Yu, H. Chen, F. J. DiSalvo, H. D. Abruña. Yolk-shell structure of polyaniline-coated sulfur for lithium-sulfur batteries. J Am Chem Soc. 2013; 135:16736–16743.

[51] C. Barchasz, F. Molton, C. Duboc, J. C. Leprêtre, S. Patoux, F. Alloin. Lithium/sulfur cell discharge mechanism: an original approach for intermediate species identification. Anal Chem. 2012;84:3973–3980.

[52] D. Marmorstein, T. H. Yu, K. A. Striebel, F. R. McLarnon, J. Hou, E. J. Cairns. Electrochemical performance of lithium/sulfur cells with three different polymer electrolytes. J Power Sources 2000;89:219–226.

[53] J. Song, T. Xu, M. L. Gordin, P. Y. Zhu, D. P. Lv, Y. B. Jiang,Y. S. Chen, Y. H. Duan, D. H. Wang. Nitrogen-doped mesoporous carbon promoted chemical adsorption of sulfur and fabrication of high-areal-capacity sulfur cathode with exceptional cycling stability for lithium-sulfur batteries. Adv Funct Mater. 2014;24:1243–1250.